The Environment of Fe3+/Fe2+ Cations in a Sodium Borosilicate Glass

WRIGHT, Adrian C., SINCLAIR, Roger N., SHAW, Joanna L., HAWORTH, Richard, BINGHAM, Paul <http://orcid.org/0000-0001-6017-0798>, FORDER, Sue, HOLLAND, Diane, SCALES, Charlie R., CUELLO, Gabriel J. and VEDISHCHEVA, Natalia M.

Published version

WRIGHT, Adrian C., SINCLAIR, Roger N., SHAW, Joanna L., HAWORTH, Richard, BINGHAM, Paul, FORDER, Sue, HOLLAND, Diane, SCALES, Charlie R., CUELLO, Gabriel J. and VEDISHCHEVA, Natalia M. (2017). The Environment of Fe3+/Fe2+ Cations in a Sodium Borosilicate Glass. Physics and Chemistry of Glasses : European Journal of Glass Science and Technology Part B, 58 (3), 78-91.

Copyright and re-use policy

N.B. Characters highlighted in red need a bar over the top.

The environment of Fe^{3+}/Fe^{2+} cations in a sodium borosilicate glass

Adrian C. Wright, Roger N. Sinclair,† Joanna L. Shaw, Richard Haworth*

J.J. Thomson Physical Laboratory, University of Reading, Whiteknights, Reading, RG6 6AF, UK

Paul A. Bingham, Susan D. Forder‡

Materials and Engineering Research Institute, Sheffield Hallam University, Howard Street, Sheffield, S1 1WB, UK

Diane Holland

Physics Department, Warwick University, Coventry, CV4 7AL, UK

Charlie R. Scales

NNL, Central Laboratory, Sellafield, Seascale, Cumbria, CA13 1PG, UK

Gabriel J. Cuello

Institut Laue-Langevin, 6 Rue Jules Horowitz, B.P. 156, 38042 Grenoble Cedex 9, France

Natalia M. Vedishcheva

Institute of Silicate Chemistry of the Russian Academy of Sciences, Nab. Makarova 2, St. Petersburg, 199034, Russia

Manuscript received

Revised version received

Accepted

The neutron diffraction isotopic substitution technique is employed to investigate the environment of Fe^{3+}/Fe^{2+} cations in a sodium borosilicate glass matrix of composition $0{\cdot}210Na_2O.0{\cdot}185{}^{11}B_2O_3.0{\cdot}605SiO_2$. The neutron diffraction data were obtained using the D4c diffractometer at the Institut Laue-Langevin (ILL; Grenoble, France), and were recorded for three samples; the base glass, the base glass incorporating natural Fe_2O_3 (12 mol%) and a similar glass containing Fe_2O_3 enriched in ^{57}Fe. The data are Fourier transformed to yield the real-space total correlation function, T(r)*, and the first co-ordination shells of the Fe^{3+}/Fe^{2+} cations are investigated via a peak fit to the isotopic difference correlation function $\Delta T_{Fe}(r)$. It is concluded that the iron is mainly present as Fe^{3+} cations, both tetrahedrally and octahedrally co-ordinated by oxygen atoms, plus a small fraction (0·07±0·01) of Fe^{2+} cations in octahedral co-ordination. The Fe^{3+} tetrahedral fraction is 0·45±0·10, and appears to exist as $FeØ_4^-$ structural units incorporated into the network of silicate chemical groupings, with their negative charge being balanced by Na^+ network modifying cations. The remaining Fe^{3+} cations (fraction 0·48±0·10) are thought to be predominantly octahedrally co-ordinated and associated with BO_3^{3-} orthoborate anions in $FeBO_3$*

chemical groupings, which become non-stoichiometric due to the reduction of some of the Fe^{3+} cations to Fe^{2+}.

Footnote

Based on a paper presented at the 2012 Society of Glass Technology Annual Meeting, Murray Edwards College, University of Cambridge, 5–7 September 2012.

* Corresponding author. Email a.c.wright@reading.ac.uk

† Deceased: 18th June 2007.

‡ Deceased: 17th July 2016.

1. Introduction

A detailed knowledge of the environment of transition metal and rare earth cations in conventional network glasses is extremely important for a number of reasons. They are added to such glasses to provide specific properties for chosen applications, e.g. desired colouring, and are also important components of the nuclear waste that is incorporated into borosilicate glasses for immobilisation/storage. In each case the important properties, for example laser line shape or the leachability of highly radioactive waste, depend on their detailed structural environment.

The present study forms part of a programme to investigate the environment of transition metal and rare earth cations incorporated into borosilicate glasses that model those employed by BNFL for the vitrification of nuclear waste. NMR, Raman and Mössbauer spectroscopy data have already been recorded by Holland and co-workers[1–3] for a $0{\cdot}103Li_2O.0{\cdot}106Na_2O.0{\cdot}186B_2O_3.0{\cdot}605SiO_2$ base glass containing equal amounts of Li_2O and Na_2O, to which has been added up to 12 mol% Fe_2O_3. They reported the presence of both tetrahedral Fe^{3+} and octahedral Fe^{2+}, with the latter fraction decreasing from ~0·22 in a glass with 2·4 mol% Fe_2O_3 to ~0·12 in the 12 mol% Fe_2O_3 glass. Raman spectroscopy showed that the fraction of $Si^{[3]}$ silicon species decreased from 0·23±0·03 to 0·18±0·03 on adding 12 mol% Fe_2O_3 to the base glass, and this was accompanied by a reduction in cationic conductivity and an increase in corrosion resistance. Reference 3 also includes a review of previous NMR studies of borosilicate glasses used for the immobilisation of nuclear waste.

Fe_2O_3 is a typical nuclear waste component from the transition metal oxides and, in this paper, the neutron diffraction isotopic substitution technique is used to investigate the environment of Fe^{2+}/Fe^{3+} cations in a borosilicate glass that also includes 12 mol% Fe_2O_3. However, the Li_2O in the above base glass has been replaced by Na_2O, to avoid the high neutron absorption cross-section of ^6Li, the modified base glass composition being $0{\cdot}210Na_2O.0{\cdot}185{}^{11}B_2O_3.0{\cdot}605SiO_2$. This same modified base glass similarly features in an accompanying study[4] of the environment of a representative rare earth (Dy^{3+}) cation, following the addition of 13 mol% Dy_2O_3.

The neutron diffraction experiment employs the first-order difference between samples containing natural Fe and Fe enriched in ^{57}Fe, as in a similar investigation[5] of the environment of the same cations in a soda–lime–silica glass. The Fe^{2+} cation fraction is determined by Mössbauer spectroscopy, and the distribution of basic structural unit species in the base glass is investigated by magic-angle-spinning (MAS) NMR spectroscopy, supported by thermodynamic modelling based on the model of associated solutions[6]. The use of both NMR spectroscopy, via the model of Dell *et al*[7] (Section 1.1), and thermodynamic modelling in unravelling the complexities of neutron diffraction data for sodium borosilicate glasses has already been addressed in a series of papers[8–10] discussing the structure of four glasses of composition $2Na_2O.2B_2O_3.SiO_2$, $Na_2O.B_2O_3.SiO_2$,

$Na_2O.B_2O_3.6SiO_2$ and $Na_2O.B_2O_3.8SiO_2$, to which the reader is directed for more detailed information.

1.1. Chemical nanoheterogeneity

An extremely important aspect of the structure of multicomponent glasses is that they exhibit chemical nanoheterogeneity in the form of composition fluctuations. In the case of alkali borosilicate glasses, this nanoheterogeneity involves silica-rich and alkali borate-rich regions and hence it is important to determine whether the transition metal and/or rare earth cations are associated with the silicate or borate component, since the latter is likely to be much more easily leached. It should be emphasised that these fluctuations are not phase separation, but rather represent compositional fluctuations that define the chemical structure of the glass, and are in excess of those expected for a network characterised by a spatially random distribution of borate and silicate basic structural units.
On the basis of ^{11}B NMR data, Dell *et al*[7] have proposed a model for the chemical structure of sodium borosilicate glasses, based on the parameters

$R=x_{Na2O}/x_{B2O3}$ (1)

and

$K=x_{SiO2}/x_{B2O3}$ (2)

where x_{Na2O}, x_{B2O3} and x_{SiO2} are, respectively, the mole fractions of Na_2O, B_2O_3 and SiO_2. According to their model, which is limited to $K\leq 8$, the chemical structure is defined by four regions incorporating the following chemical groupings:

1. $\{R<½\}$: $Na_2O–B_2O_3+SiO_2$

2. $\{½\leq R\leq(½+K/16)\}$: $Na_2O.2B_2O_3$(sodium diborate)$+Na_2O.B_2O_3.8SiO_2$(*"reedmergnerite"*)$+SiO_2$

3. $\{(½+K/16)\leq R\leq(½+K/4)\}$: $Na_2O.2B_2O_3+xNa_2O.B_2O_3.8SiO_2$

and

4. $\{(½+K/4)\leq R\leq(2+K)\}$: $Na_2O.2B_2O_3+2Na_2O.B_2O_3$(sodium pyroborate)$+2\cdot 5Na_2O.B_2O_3.8SiO_2+Na_2O.SiO_2$(sodium metasilicate).

The $Na_2O.2B_2O_3$ chemical groupings involve equal numbers of $BØ_3$ and $BØ_4^-$ basic structural units, where Ø represents a bridging oxygen atom, but these do not necessarily combine to form diborate superstructural units, whilst the so-called *"reedmergnerite groups"* comprise a $BØ_4^-$ tetrahedron linked to four $SiØ_4$ tetrahedra plus an Na^+ network-modifying cation, yielding the composition $Na_2O.B_2O_3.8SiO_2$. Note, however, that this is ***not*** the composition ($Na_2O.B_2O_3.6SiO_2$) of the compound reedmergnerite. The $xNa_2O.B_2O_3.8SiO_2$ and $2\cdot 5Na_2O.B_2O_3.8SiO_2$ chemical groupings consist of *"modified reedmergnerite groups"* with extra Na^+ network-modifying cations associated with nonbridging oxygen atoms on the silicate ($SiOØ_3^-$) tetrahedra surrounding the central $BØ_4^-$ tetrahedron. Of particular interest, in respect of the incorporation of the Fe_2O_3 into the present base glass, are the pyroborate ($B_2O_5^{4-}$) anions in the $2Na_2O.B_2O_3$ chemical groupings in Region 4, as will become apparent in Section 4.3.

2. Experimental procedure

2.1. Sample preparation

The base glass, of composition $0{\cdot}210Na_2O.0{\cdot}185^{11}B_2O_3.0{\cdot}605SiO_2$, was prepared using boric acid enriched (99·27%) in ^{11}B, to avoid the high neutron absorption cross-section of ^{10}B. Powdered sodium carbonate, enriched boric acid and silica were tumbled for approximately 2 h, and then heated with the furnace to 1350°C, in air in a platinum–rhodium (~10% Rh) crucible, at a rate of 300°C/h. The sample was quenched to the vitreous state in water and dried overnight in a drying oven, before being powdered. The enriched ^{57}Fe isotope was the same as that in Table 2 of Ref. 5, and has a neutron scattering length of $(0{\cdot}284\pm0{\cdot}010)\times10^{-14}$ m, compared to $(0{\cdot}945\pm0{\cdot}002)\times10^{-14}$ m for ^{NAT}Fe.[11] A full set of neutron scattering lengths is given in Table 1, together with the atom fractions, x_i, for both the base and Fe_2O_3-containing glasses. Similar quantities of the two Fe_2O_3-containing samples were prepared simultaneously, in the same furnace, to ensure that they were identical except for the different Fe isotopic compositions. High purity $^{NAT}Fe_2O_3$ and $^{57}Fe_2O_3$ (12 mol.%) were mixed with the base glass (88 mol%) and heated with the furnace to 1350°C at a rate of 10°C/min, and then held at 1350°C for 1 h, before quenching into water and drying overnight. The atomic number densities, ρ°, of the base and ^{NAT}Fe-containing glasses were determined from helium pycnometry to be 0·08116±0·00006 and 0·07821±0·00002 atom $Å^{-3}$, respectively.

2.2. Experimental techniques

Neutron diffraction patterns were recorded for the base glass and the Fe_2O_3-containing samples using the D4c diffractometer[12,13] on the high-flux reactor at the Institut Laue-Langevin, at an incident wavelength of 0·5021±0·0001 Å. The data reduction closely followed that of Ref. 5, and is illustrated for the ^{NAT}Fe-containing sample in Figure 1, which shows the raw diffraction pattern (points) plus cubic spline fit (solid line), the corrected, normalised diffraction pattern, $I(Q)$ (solid line) and the nuclear+paramagnetic self-scattering, $I^S(Q)+I^M(Q)$ (dashed line), and the interference function, $Qi(Q)$. The magnetic form factor, $f^M(Q)$, for the Fe^{3+} cations was generated from the coefficients tabulated by Brown.[14]

The experimental techniques and data reduction for the Mössbauer specroscopy and ^{29}Si MAS NMR spectroscopy were the same as those in Ref. 5. Fits to the Mössbauer spectrum were carried out using two different methods. The first fitted two Lorentzian doublets for Fe^{3+} and one for Fe^{2+}, as shown in Figure 2(A). The second used the extended Voigt-based fitting (*x*VBF) method: one doublet was fitted for Fe^{3+} and one for Fe^{2+}, as shown in Figure 2(B). The Fe^{2+} fractions obtained from these fits (Lorentzian fit, 0·072±0·020; xVBF fit, 0·083±0·020) agree well within the fitting uncertainty, and can be compared to the value of 0·115±0·005 reported by Parkinson *et al*[1] for their glass in which half of the Na_2O has been replaced by Li_2O (*cf.* Section 1). The small measured differences in iron redox between the present fits and those reported by Parkinson *et al*[1] can be attributed to differences in alkali oxide constituents, melting times and/or melting temperatures. The atom fractions in Table 1 and the value of ρ° for the Fe-containing samples include allowance for the Fe^{2+} content.

^{11}B MAS NMR spectra were obtained for the base glass at 14·1 T using a Bruker 600 MHz Avance II+ spectrometer operating at 192·3 MHz. A 4 mm Varian T3 probe was used with MAS frequency 12 kHz; pulse width 1 μs (~π/12) and pulse delay 4 s. The ^{11}B MAS NMR spectrum was referenced against solid BPO_4 taken as −3·3 ppm with respect to the primary reference $Et_2O{:}BF_3$, and peak fits were performed using the program DMfit2009.[15]

2.3. Thermodynamic modelling

Given the complexity of the interpretation of both the neutron diffraction and MAS NMR data, a thermodynamic modelling study was undertaken to predict the distribution of the basic structural

unit species in the base glass, using the model of associated solutions.[6] Calculations of the chemical structure (Table 2) were performed in the same way as those for the sodium borosilicate system in Refs 9 and 16–18, and the resulting distribution of structural unit species is given in Table 3. The thermodynamic modelling data in Table 3 are presented in two different ways, *viz.* separate fractions for the borate and silicate structural units, as normally quoted in NMR studies, and the combined fractions, which more accurately represent the overall structure. {See, for example, Equations (24) and (26) of Ref. 17.}

It is important to note that the derivation of the chemical structure (equilibrium fractions of the various chemical groupings) in Table 2, via the model of associated solutions,[6] is entirely rigorous, in that it does not involve any adjustable parameters, being solely defined by the minimum Gibbs free energy for the system as a whole. The conversion of the chemical structure in Table 2 into the structural unit fractions of Table 3 is based on the assumption that the short-range structures of the chemical groupings (i.e. the structural units present) are similar to those of the corresponding crystalline phases.

3. Results

3.1. Neutron diffraction

The corrected, normalised diffraction patterns, $I(Q)$, for all three samples are shown in Figure 3, and the data were Fourier transformed (Q_{max}=23·4 Å^{-1}) to give the corresponding real-space total correlation functions, $T(r)$. The correlation functions for the two Fe_2O_3-containing glasses are shown in Figure 4, together with their difference,

$$\Delta T(r)=x_{Fe}\Delta T_{Fe}(r)^{*} \qquad (3)$$

where $\Delta T_{Fe}(r)$ is the Fe–Fe+Fe–X (X=Na, B, Si or O) difference correlation function, and that for the base glass is in Figure 5, which also includes the Fe–Fe+X–X difference correlation function, $\Delta T_X(r)$. The difference, $\Delta T(r)$, between $\Delta T_X(r)$ and the correlation function for the base glass, also plotted in Figure 5, provides information on the modification of the base glass structure as a result of the introduction of the Fe_2O_3 (see Section 4.3). Comparing to the base glass (Figure 5), the contribution from the Fe–O bonds can be clearly seen on the high-r side of the first (B–O+Si–O) peak in $T(r)$ for the Fe_2O_3-containing samples in Figure 4.

3.2. Base glass

The composition of the base glass yields values for R and K of 1·14 and 3·27, respectively, which locates it in Region 3 of the Dell *et al*[7] model, and leads to a chemical structure of the form

$$x_D(Na_2O.2B_2O_3)+x_R(xNa_2O.B_2O_3.8SiO_2)=0{\cdot}42(Na_2O.2B_2O_3)+0{\cdot}58(2{\cdot}05Na_2O.B_2O_3.8SiO_2) \qquad (4)$$

in which x_D=0·42 and x_R=0·58 are the fractions of the sodium diborate and *"modified reedmergnerite"* chemical groupings. The results of the thermodynamic modelling have already been given in Tables 2 and 3 (Section 2.3), and present a much more complete picture of the overall structure than that of the Dell *et al*[7] model, which only considers the borate subnetwork. Thus, in addition to $Na_2O.2B_2O_3$ and $Na_2O.B_2O_3.6SiO_2$, the former reveals significant fractions of $Na_2O.B_2O_3.2SiO_2$, $Na_2O.2SiO_2$ and unreacted SiO_2 (Table 2), together with minor fractions of $Na_2O.3B_2O_3$, $Na_2O.B_2O_3$, $3Na_2O.8SiO_2$, and $Na_2O.SiO_2$. Note that the *"modified reedmergnerite"*

[*] $\Delta T_{Fe}(r)$ and $\Delta T_X(r)$ are defined in Ref. 5.

($Na_2O.B_2O_3.8SiO_2$) composition of the Dell *et al*[7] model is required to compensate for the absence of $Na_2O.2SiO_2$ and unreacted SiO_2, and that the thermodynamic modelling indicates the presence of two sodium borosilicate chemical groupings, reedmergnerite ($Na_2O.B_2O_3.6SiO_2$) and danburite ($Na_2O.B_2O_3.2SiO_2$).

As demonstrated by the thermodynamic modelling, more than two silicon species are expected for the base glass because of the possibility of Si–Ø–B linkages, in addition to the formation of nonbridging oxygen atoms. Therefore, a simulation of the ^{29}Si NMR peaks was undertaken, based on the predictions of the Dell *et al*[7] model and the thermodynamic modelling, plus evidence from the ^{11}B NMR spectroscopy. Figure 6 shows the ^{29}Si spectrum obtained from the base glass accompanied by the Gaussian lines used to fit the spectrum to contributions from $Si^{[4]}$(*n*B) and $Si^{[3]}$ species. Both of these species are approximately axially symmetric and therefore each centreband has associated spinning sidebands. Fitting of the sidebands to two contributions could only be achieved by constraining their half-widths to be close to those of the centre bands. The fitted peak parameters are summarised in Table 4.

The ^{11}B spectrum (Figure 7) is typical of spectra reported for glasses of similar composition; i.e. with similar values of *R* (1·14) and *K* (3·27).[3] The two peaks in the spectrum are from boron nuclei in 4-coordinated (~0 ppm) and 3-coordinated sites (~17 ppm). The fraction, x_4, of the boron atoms that are 4-fold co-ordinated can be obtained by integrating the area under the $B^{[4]}$ peak and taking its ratio to the area under the entire central (½↔–½) spectrum. However, the area under the 3-coordinated boron $B^{[3]}$ peak has to be corrected for loss of signal into the satellite transitions.[19] At high fields and rapid rotation, this correction is small (~4%) and a final value of 0·75±0·04 is obtained for x_4. The Dell *et al*[7] model predicts that

$$x_4 = ½ + K/16 = 0·704 \qquad (5)$$

for this composition. There are in fact several contributions to the $B^{[4]}$ and $B^{[3]}$ peaks. In their studies of similar sodium borosilicates, Du & Stebbins[20] fitted peaks to sites corresponding to $B^{[3]}_{ring}$, $B^{[3]}_{non\text{-}ring}$ and $B^{[4]}$ with different numbers of next-nearest neighbour silicon atoms, namely $B^{[4]}$(B,3Si) and $B^{[4]}$(4Si). In the case of the $B^{[4]}$ peak manifold, the values of the quadrupole coupling constant, C_Q, are small, and the individual peak line shapes can be approximated as Gaussian–Lorentzian, with the Gausian:Lorentzian ratio fixed at 0·7. Two peaks were used to simulate the $B^{[4]}$ contribution. The values of C_Q for the $B^{[3]}$ peaks are typically ~2·5 MHz, and thus the $B^{[3]}$ manifold must be simulated using two quadrupole line peak shapes, with asymmetry parameter, η_Q, fixed at 0·2, representing $B^{[3]}_{ring}$ and $B^{[3]}_{non\text{-}ring}$. Table 5 presents the results of this peak fitting. The parameters shown are reasonable consistent with those from Du & Stebbins,[20] given that their nearest sodium borosilicate composition to the current study has *K*=4 and *R*=0·75.

There are five possible contributions to the first peak in $T(r)$ for the base glass, *viz.* from B–Ø and $B–O^-$ bonds for trigonal boron atoms, from B–Ø bonds for tetrahedral boron atoms, and from Si–Ø and $Si–O^-$ bonds, where O^- represents a negatively-charged nonbridging oxygen atom. The situation is further complicated by the systematic variation of the bond lengths both within borate and silicate basic structural units, and when borate structural units are incorporated into superstructural units, as discussed in Refs 10, 21 and 22. The extent of this variation can be seen from Table 6, which shows the average bond lengths for independent borate and silicate structural units, calculated from the data for crystalline B_2O_3, SiO_2, alkali borates, alkali silicates and reedmergnerite in Table 2 of Ref. 10. Hence there are too many overlapping peaks to extract meaningful bond lengths, root mean square (RMS) bond length variations and co-ordination numbers for each contribution. It was

therefore decided to perform a two-peak fit, to provide a guide as to the changes in the structure of the base glass occurring on the introduction of the Fe_2O_3.

The two-peak fit to the base glass is shown in Figure 8(A), and the peak parameters are summarised in Table 7. However, whilst the lower-*r* peak from this fit will be dominated by B–Ø and B–O^- bonds, and the higher-*r* peak by Si–Ø and Si–O^- bonds, peak overlap/intermixing means that these peaks cannot be ascribed to a particular bond type, which means that the uncertainties in the individual peak parameters are irrelevant, and hence are not quoted in Table 7. It is important to note that the fit involves two ***symmetric*** peaks, whereas the peaks arising from the borate and silicate basic structural units will certainly not be symmetric, due to the presence of more than one type of bond in each case. The quality/accuracy of the fit is given by the R_χ factor (Table 7), and can be seen from the peak fit residual {Figure 8(A)}. For convenience, henceforth the lower-*r* peak will be referred to as the B(O) peak and the higher-*r* peak as the Si(O) peak, even though there is almost certainly some intermixing. No attempt was made to fit the second peak in $T(r)$, which includes contributions from Na^+–O^- bonds to nonbridging oxygen atoms, Na^+–Ø distances and O–O distances within the various borate and silicate structural units. The results of the two-peak fit will be discussed in Section 4.3, together with a similar fit to $\Delta T_X(r)$ {Figure 8(B)}.

3.3. Fe–Fe+Fe–X correlation function

As in Ref. 5, the calculation of the difference, $x_{Fe}\Delta T_{Fe}(r)$, between the correlation functions for the ^{NAT}Fe- and ^{57}Fe-containing samples included a small (~2%) renormalisation of the diffraction pattern for the ^{57}Fe-containing glass, due to the extremely large uncertainty (30%; *cf.* Table 2 of Ref. 5) on the total scattering cross-section for the ^{57}Fe isotope. The Fe–Fe+Fe–X correlation function, $\Delta T_{Fe}(r)$, is non-zero after the first (Fe–O) peak, suggesting that there is no well-defined cut-off distance for the first Fe(O) co-ordination shell. The peaks at ~3·25 and ~4·4 Å are mainly due to Fe–B/Si/Na and Fe–(2)O interactions, respectively. A 2-peak fit (Figure 9 and Table 8) to the first Fe–O peak gives a total co-ordination number, $n_{Fe(O)}$, of 4·88±0·20, the increased uncertainty being due to that on the neutron scattering length for the ^{57}Fe isotope of $\pm 0{\cdot}01\times10^{-14}$ m (Table 1). The average Fe–O bond lengths, $r_{Fe–O}$, are 1·895 Å {between tetrahedral (1·85 Å) and either 5-fold (1·94 Å) or octahedrally (2·00 Å) co-ordinated Fe^{3+} – see Table 1 of Ref. 5} and 2·182 Å {(*cf.* 5-fold (2·06 Å) and octahedrally (2·14 Å) co-ordinated Fe^{2+} cations}, respectively, the root mean square (rms) bond-length variations, $\langle u_{Fe–O}^2\rangle^{½}$, being 0·079 and 0·041 Å.

The 2-peak fit in Figure 9 does not include all of the area between the first and second peaks, as may be seen from the peak-fit residual. This extra area may include contributions from longer Fe–O bonds, Fe–Fe and/or Fe–X distances. As in Ref. 5, therefore, a further fit was performed, adding an extra broad {$\langle u_{Fe–O}^2\rangle^{½}$=0·2 Å} peak at 2·48 Å, such that the low-*r* tail of the peak at ~3·25 Å reduced smoothly to zero at ~2·55 Å. The assignment of at least part of this extra area to longer Fe–O bonds is consistent with the longest Fe–O bond length of 2·537 Å (octahedral Fe^{3+} cations) in iscorite (Fe_7SiO_{10}),[23] whilst the total area corresponds to an increase in the total average Fe(O) co-ordination number to 5·34. The Fe(O) co-ordination number was also estimated from the integrated area under $r\Delta T_{Fe}(r)$, assuming that all of this area is due to Fe–O bonds (*cf.* Ref. 5). The running co-ordination number from 1·5 Å to *r* is shown in Figure 10, as a function of *r*. The minimum in $r\Delta T_{Fe}(r)$ is at ~2·46 Å; and the average co-ordination number for the range 1·50–2·46 Å is 5·00.

3.4. Fe–Fe+X–X correlation function

The Fe–Fe+X–X first-order difference correlation function, $\Delta T_X(r)$, is plotted in Figure 5, divided by the base glass fraction (0·88). This is to allow subtraction of the base glass correlation function to give the curve denoted $\Delta T(r)$, which can be interpreted in terms of the change in the structure of the base glass caused by the introduction of Fe_2O_3. As in the case of $\Delta T_{Fe}(r)$, it was necessary to apply the same correction to the magnitude of the correlation function for the ^{57}Fe-containing sample. The Fe–Fe+X–X correlation function shows the first peak in $T(r)$ for the Fe-containing glass without interference from the Fe–O peak, and so a two-peak fit {Figure 8(B)} was performed, similar to that for the base glass, the parameters being given in Table 7.

4. Discussion

4.1. Structure of base glass

Denoting the overall structural unit fractions in the base glass as x_{B4}, x_{B3}, x_{B2}, x_{Si4}, x_{Si3} and x_{Si2}, where the subscript indicates the network-forming cation plus the number of bridging oxygen atoms, the total number of negative charges per composition unit (c.u.) is equal to the number of Na^+ cations per c.u.:

$$2x_{Na2O}=x_{B4}+x_{B2}+x_{Si3}+2x_{Si2}=0{\cdot}420 \quad (6)$$

The ^{11}B NMR data indicate that the fraction of the boron atoms, x_4, that are tetrahedrally co-ordinated is

$$x_4=x_{B4}/2x_{B2O3}=0{\cdot}75\pm0{\cdot}04 \quad (7)$$

This is slightly higher than the value (0·72±0·03) obtained from the thermodynamic modelling, and higher than predicted by the Dell *et al*[7] model, but there is no evidence for the existence of $BO\emptyset_2^-$ basic structural units within the experimental uncertainty. It is also higher than the 0·69±0·04 observed for the waste-form glass in which half of the Na_2O is replaced by Li_2O,[3] although this reflects the findings of the study by Zhong *et al*[24] that x_4 is significantly smaller (typically 25% less for the present values of K and R) for lithium borosilicate as compared to sodium borosilicate glasses.

If it is assumed that neither $BO\emptyset_2^-$ nor $SiO_2\emptyset_2^{2-}$ structural units are present, then the ^{11}B NMR data yield

$$x_{B4}=2x_4x_{B2O3}/(2x_{B2O3}+x_{SiO2})=0{\cdot}285\pm0{\cdot}015 \quad (8)$$

$$x_{B3}=2x_{B2O3}/(2x_{B2O3}+x_{SiO2})-x_{B4}=0{\cdot}094\pm0{\cdot}015 \quad (9)$$

$$x_{Si3}=2x_{Na2O}/(2x_{B2O3}+x_{SiO2})-x_{B4}=0{\cdot}146\pm0{\cdot}015 \quad (10)$$

and

$$x_{Si4}=x_{SiO2}/(2x_{B2O3}+x_{SiO2})-x_{Si3}=0{\cdot}475\pm0{\cdot}015 \quad (11)$$

A comparison of these structural unit fractions with those from the thermodynamic modelling in Table 3 reveals excellent agreement, well within their combined uncertainties. Thus approximately $^2/_3$ of the Na^+ cations are associated with $B\emptyset_4^-$ tetrahedra, and $\sim^1/_3$ are compensated by nonbridging oxygen atoms on $SiO\emptyset_3^-$ structural units. This is in accordance with the chemical natures of B_2O_3 and SiO_2, in that the alkaline oxide, Na_2O, preferably interacts with the more acidic B_2O_3, rather than the less acidic SiO_2.

The relative intensities (Table 4) of the two fitted peaks (including sidebands) in the ^{29}Si spectrum in Figure 6 are consistent with the above values of x_{Si3} (0·146) and x_{Si4} (0·475), which correspond to approximate $Si^{[3]}$ and $Si^{[4]}$ fractions of 0·23 and 0·77, respectively. The chemical shifts observed are also close to the values reported in the literature. $Si^{[3]}$ is generally quoted as having a shift of about −90 ppm and Bunker *et al*[25] reported a chemical shift of −105 ppm for $Si^{[4]}$(B,3Si) compared to −110 ppm for $Si^{[4]}$(4Si). Table 9 shows the results of calculating the average Si(B) co-ordination number using the thermodynamic prediction of the chemical groupings present, assuming that the $Si^{[4]}$ species in silica have zero boron next-nearest neighbours whilst those in the danburite and reedmergnerite groupings have the same n_{SiB} as $Si^{[4]}$ in the crystals (3 and 4/3, respectively). It also assumes that any $Si^{[4]}$…$B^{[3]}$ next nearest neighbours can be neglected, i.e. that $B^{[3]}$ structural units are part of the borate network only. The peaks in the ^{29}Si NMR spectrum of the base glass can then be assigned as follows: The peak at −88 ppm consists of the $Si^{[3]}$ contribution with $Si^{[2]}$ being too weak to discriminate. It is thought that the nonbridging oxygen on the $Si^{[3]}$ structural unit makes it unlikely that the negatively charged $B^{[4]}$ units would be a neighbouring unit, and so $Si^{[3]}$(B) can be neglected at this composition. The peak at −100 ppm in Figure 6 contains the $Si^{[4]}$ contributions from the chemical groupings indicated in Table 9, each of which provides a different value for n_{SiB}. There is insufficient information in the spectrum to be able to discriminate the individual contributions, but the centre of gravity of the peak can be estimated from the chemical shifts of the spectra of the pure chemical groupings, weighted by the relative abundances of their various $Si^{[4]}$ units. The relevant chemical shifts can be taken as −110 ppm for $Si^{[4]}$ in silica; −102 ppm for $Si^{[4]}$ in reedmergnerite {a mix of $Si^{[4]}$(B,3Si) and $Si^{[4]}$(2B,2Si)}, and −90 ppm for $Si^{[4]}$(3B,Si) in danburite. The values for reedmergnerite and danburite were determined for vitreous sodium preparations[26] of the two compounds, although these are not ideal analogues, since they contain ~30% $B^{[3]}$. The contribution from trisodum octasilicate is considered insignificant. The calculated centre of gravity of the composite peak is therefore at −101±2 ppm, consistent with the observed −100±1 ppm.

4.2. Fe^{2+}/Fe^{3+} cation environment

The Mössbauer spectroscopy has confirmed that the iron in the present glasses is highly oxidised, such that the Fe^{2+} fraction is only 0·072±0·020 (Lorentzian fit) or 0·083±0·020 (*x*VBF fit), with the large majority of the iron being present as Fe^{3+}. The Fe^{2+} fraction has been calculated from the spectral areas, and assumes that the recoil-free fraction is the same for Fe^{2+} and Fe^{3+} cations in these glasses. The spectrum was satisfactorily fitted by both methods. The first used three Lorentzian doublets; one representing the Fe^{2+} and two the Fe^{3+} cations. The centre shifts (CS) obtained for the two Fe^{3+} doublets are 0·13±0·02 and 0·35±0·02 mm s^{-1}. The first CS (fractional area 0·340) is nearer the lower boundary of the tetrahedral regime (0·10–0·35 mm s^{-1} [27]), and the second (fractional area 0·588) is at the upper boundary of the tetrahedral regime and close to the lower boundary for Fe^{3+} in octahedral co-ordination (0·3–0·5 mm s^{-1} [27]). Quadrupole splitting (QS) and linewidth (LW) parameters for the two Fe^{3+} doublets are (doublet 1) 0·96±0·02 and 0·19±0·02 mm s^{-1}, and (doublet 2) 0·96±0·02 and 0·24±0·02 mm s^{-1}, respectively. The CS, QS and LW for the Fe^{2+} doublet are 0·95±0·02 mm s^{-1}, 2·16±0·02 mm s^{-1} and 0·25±0·02 mm s^{-1}. The alternative fitting of the Mossbauer spectra, using extended Voigt-based fitting (*x*VBF), shown in Figure 2(B), involves two doublets, one for Fe^{3+} and one for Fe^{2+}, the Lorentzian HWHM linewidths being 0·16 mm s^{-1}. The Fe^{3+} doublet yields CS=0·26±0·02 mm s^{-1}, with sigma=0·11 mm s^{-1}; QS=0·94±0·02 mm.s^{-1}, with sigma=0·25 mm s^{-1}, and a fractional area of 0·9172. The Fe^{2+} doublet has

CS=0·82±0·02 mm s^{-1}, with sigma constrained at 0·20 mm s^{-1}; QS=2·22±0·02 mm s^{-1}, with sigma constrained at 0·20 mm s^{-1}, and a fractional area of 0·0828. Arguably, the quality of fit is greater for the *x*VBF model than the Lorentzian model. This is consistent with the presence of a distribution of co-ordination sites which can be better represented by an xVBF model. The fitted CS and QS parameters from the *x*VBF fit are consistent with a major proportion of Fe^{3+} cations occupying tetrahedrally-coordinated sites[27], although the values of sigma also support the presence of some fraction of higher co-ordinated sites which can be expected to be 5- and/or 6-fold co-ordinated. For both the Lorentzian and *x*VBF models, the CS and QS for the fitted doublets, the relative doublet areas, and their associated linewidths combine to indicate a distribution of site parameters around an average co-ordination number for the Fe^{3+} cations of circa 5, and an average co-ordination number for the Fe^{2+} cations of ~6. These results are entirely consistent with those from the neutron diffraction data.

The site distributions for iron in glasses have received considerable attention in the literature, but it is important to realise that such studies have considered a wide range of glass compositions, iron contents, and redox conditions, and so direct comparisons must be carried out with caution. Wilke *et al*[28] have studied the Fe(O) co-ordination number for Fe^{2+} and Fe^{3+} cations in a wide range of minerals, and find that in the vast majority of cases these cations are in either 4- or 6-fold co-ordination. They do, however, quote one example for Fe^{2+} {grandidierite; $(Mg,Fe)Al_3(BO_4)(SiO_4)O$ (1·1 wt% FeO)} and one for Fe^{3+} {yoderite; $(Mg,Al,Fe)_8Si_4(O,OH)_{20}$ (6·1 wt% Fe_2O_3)} cations where the iron is 5-fold co-ordinated. On the other hand, there are several reports of 5-fold co-ordination in the vitreous state. For example, Rossano *et al*[29,30] have employed a combination of EXAFS spectroscopy and molecular dynamics simulations to investigate the environment of the Fe^{2+} cations in vitreous $CaO.FeO.2SiO_2$, and conclude that they occupy distorted sites, whose geometry varies continuously from a tetrahedron to a triangular bipyramid.

The work of Weigel *et al*[31,32] on the structure of vitreous $Na_2O.Fe_2O_3.4SiO_2$ has already been discussed in Ref. 5, where it is compared to that on a soda–lime–silica (0·127Na_2O.0·162CaO.0·711SiO_2) glass containing 12 mol% Fe_2O_3. Both studies conclude that the largest fraction of the iron is present as Fe^{3+} cations in tetrahedral co-ordination, but Weigel *et al*[31,32] propose that the remaining Fe^{3+}/Fe^{2+} cations are in 5-fold co-ordination, whereas Wright *et al*[5] find that they are in 6-fold co-ordination. A possible explanation of this discrepancy is given below. Weigel *et al*[33] have also investigated a series of $Na_2O.xFe_2O_3.(1-x)Al_2O_3.4SiO_2$ glasses in which Al_2O_3 is progressively substituted for Fe_2O_3, and reach the same conclusion as to the co-ordination state of the iron; i.e. 4- and 5-fold.

It is clear from the 2-peak fit to the Fe–Fe+Fe–X difference correlation function discussed in Section 3.3 that the accuracy to which the Fe^{2+}/Fe^{3+} cation environments can be deduced is limited by the assignment given to the extra area between the first and second peaks in $\Delta T_{Fe}(r)$. First, therefore, the 2-peak fit will be considered in isolation, and then the possible interpretations of this extra area. In analysing the co-ordination numbers in Table 8, it is important to understand that they are the co-ordination numbers averaged over ***all*** of the Fe atoms in the sample. The second peak from the 2-peak fit is at 2·182 Å, which is at a significantly higher *r* than the mean Fe^{2+}–O bond length (2·14 Å) for octahedral co-ordination in Table 1 of Ref. 5. If the assignment of this peak solely to Fe^{2+}–O bonds were correct, the Fe^{2+} cation fraction of 0·072 would yield an Fe^{2+}(O) co-ordination number of 8·1 (0·58/0·072), greatly in excess of the expected value of 6·0; i.e. this peak must also include a contribution from Fe^{3+}–O bonds. It can, however, be concluded that the vast majority of the Fe^{2+} cations are likely to be in octahedral co-ordination. The position of the first peak (1·895 Å) indicates that a significant fraction of the Fe^{3+} cations must be in tetrahedral co-ordination but, to extract their fraction, it is necessary to consider the total area under the two peaks,

which yields an overall average Fe(O) co-ordination number of 4·88. The remainder of the Fe^{3+} cations may be in either 5-fold or 6-fold (octahedral) co-ordination. Assuming the latter leads to an upper limit for the fraction of the Fe^{3+} cations that are in tetrahedral co-ordination of 0·60. Alternatively, in terms of the ***total*** Fe content, the overall fractions are: tetrahedral Fe^{3+} 0·56; octahedral Fe^{3+}, 0·37 and octahedral Fe^{2+}, 0·07. At the opposite extreme, it is possible to assume that the remaining Fe^{3+}/Fe^{2+} cations are 5-fold co-ordinated, as proposed by Weigel *et al*[31,32] for vitreous $Na_2O.Fe_2O_3.4SiO_2$. In this case the overall average Fe(O) co-ordination number of 4·88 reduces the fraction of the Fe^{3+} cations in tetrahedral co-ordination to only 0·12, which is much lower than inferred by the Mössbauer data and the position of the first peak in the fit to $\Delta T_{Fe}(r)$.

To extract the total Fe(O) co-ordination number, Weigel *et al*[32] fit three Gaussian peaks to the real-space correlation function for their ^{NAT}Fe-containing sample (Ref. 32, Figure 2 and Table 4) to extract an average Si–O bond length of 1·63 Å, and Fe–O distances of 1·87 and 2·01 Å, the corresponding co-ordination numbers being 3·9, 3·2 and 1·0, respectively. However, the fit does not include the real space peak function, $P(r)$, and hence the peak areas (co-ordination numbers) do not include the satellite features on either side of the central maximum. Weigel *et al*[32] also performed a single-Gaussian fit to the first peak in $\Delta T_{Fe}(r)$, to yield an average Fe–O distance of 1·89 Å, and a total Fe(O) co-ordination number of 4·3 (*cf.* 4·2 for the 3-peak fit). In this connection, it is important to note that, whereas the latter peak appears symmetric, the corresponding peak in the present study is asymmetric, having a tail to high *r*, with the result that the second fitted peak is also moved to significantly higher *r* (2·182 Å). This, together with the higher average Fe(O) co-ordination number of 4·88, compared to 4·2 for vitreous $Na_2O.Fe_2O_3.4SiO_2$,[32] again indicates a large fraction of 6-fold co-ordinated Fe^{3+}/Fe^{2+} cations in the present glasses. In respect of the use of EXAFS spectroscopy in studying the environment of cations with highly distorted first co-ordination shells, it is also worth pointing out that EXAFS spectroscopy is much less sensitive to broad distributions of inter-atomic distances than are diffraction techniques[34] and hence to the presence of a high-*r* tail, such as that in Figure 9.

The Fe^{3+} tetrahedral fraction of 0·56, calculated assuming no 5-fold co-ordination, is clearly an overestimate, given the high-*r* tail of the first peak in $\Delta T_{Fe}(r)$ and the fact that $\Delta T_{Fe}(r)$ is non-zero between the first and second peaks. The most likely scenario is that the remaining Fe^{3+}/Fe^{2+} cations (i.e. excluding the tetrahedrally co-ordinated Fe^{3+} cations) have a distorted octahedral first co-ordination shell with at least some of the extra area from the 3-peak fit being due to long Fe^{3+}–O or Fe^{2+}–O bonds. If all of the extra area is assigned to Fe–O bonds, and in the absence of 5-fold co-ordination, the Fe^{3+} tetrahedral fraction is reduced to 0·33 (octahedral Fe^{3+}, 0·60 and octahedral Fe^{2+}, 0·07), but this is certainly an underestimate, since some of the extra area will be due to interactions other than Fe–O bonds. Finally, the co-ordination number from the integrated area under $r\Delta T_{Fe}(r)$ between 1·50 and 2·46 Å is 5·00 (tetrahedral Fe^{3+} 0·50; octahedral Fe^{3+}, 0·43 and octahedral Fe^{2+}, 0·07). Taken together, these thee estimates yield a "best" value for the average Fe(O) co-ordination number of 5·1±0·2, leading to the following cation fractions: tetrahedral Fe^{3+} 0·45±0·10; octahedral Fe^{3+}, 0·48±0·10 and octahedral Fe^{2+}, 0·07±0·01.

4.3. Modification of base glass structure

The effect of the addition of Fe_2O_3 on the structure of the base glass is best seen from the $\Delta T_X(r)$ – base glass difference correlation function, $\Delta T(r)$ in Figure 5. The "reverse-curve" structure in the region of the various boron–oxygen and silicon–oxygen bond lengths (maximum at 1·29 Å and minimum at 1·54 Å), together with the peak fit parameters in Table 7, strongly suggest a reduction in the fraction, x_4, of the boron atoms that are 4-fold co-ordinated, and an increase in the fraction of

trigonal borate structural units with nonbridging oxygen atoms. The minimum at 2·47 Å in $\Delta T(r)$ is also consistent with the conversion of $B\emptyset_4^-$ tetrahedra into trigonal borate structural units, in that it reflects the reduction in the number of intra-structural unit O–O distances. {The O–O distance for a regular $B\emptyset_4^-$ tetrahedron, with a B–Ø bond length of 1·468 Å (Table 6) is 2·397 Å.} The average co-ordination number for the B(O) peak is reduced from 3·89 to 3·43, and the average bond length from 1·477 to 1·427Å. These bond lengths should be compared to the average value for $B\emptyset_4^-$ tetrahedra (1·468 Å) and those for the B–O^- and B–Ø bonds in trigonal borate structural units in Table 6. On the other hand, the smaller increase in the average bond length for the Si(O) peak, from 1·617 to 1·627 Å, suggests a slight increase in the number of Si–Ø relative to Si–O^- bonds, although this may be due to a change in the level of intermixing between the two peaks. (The average Si–O^- and Si–Ø bond lengths in crystalline α-$Na_2O.2SiO_2$[35] and β-$Na_2O.2SiO_2$[36] are 1·634 and 1·579 Å, respectively.) It therefore appears that the modification of the base glass structure on the incorporation of the Fe_2O_3 mainly involves the replacement of the negatively-charged $B\emptyset_4^-$ tetrahedra with negatively-charged nonbridging oxygen atoms. This strongly suggests that the majority of the Fe^{3+}/Fe^{2+} cations are associated with borate structural units; i.e. that they are predominantly to be found in borate chemical groupings.

The peak in $\Delta T(r)$ (Figure 5) at 2·99 Å is due to the O–O distances within the Fe^{2+} and Fe^{3+} co-ordination polyhedra. Assuming the Fe–O bond lengths for silicate systems in Table 1 of Ref. 5, and regular octahedral co-ordination of the oxygen atoms around the Fe^{2+} and Fe^{3+} cations, yields O–O distances of 3·03 and 2·83 Å, respectively, whereas regular $Fe\emptyset_4^-$ tetrahedra give rise to an O–O distance of 3·02 Å. A guide as to the expected interatomic distance between the Fe^{3+} cations and the negatively-charged nonbridging oxygen atoms on the triangular borate structural units can be gleaned from the crystalline structures of ferric orthoborate, $FeBO_3$ (or $Fe_2O_3.B_2O_3$),[37,38] and Fe_3BO_6 ($3Fe_2O_3.B_2O_3$).[39,40] Ferric orthoborate[37,38] has the calcite structure, consisting of Fe^{3+} cations plus BO_3^{3-} orthoborate anions. The Fe^{3+} cations are 6-fold co-ordinated with a single Fe^{3+}–O^- distance of 2·028 Å, which for regular octahedral co-ordination yields an O–O distance of 2·87 Å, and the B–O^- bond length for the BO_3^{3-} anions is 1·379 Å[38]. The structure of Fe_3BO_6 is based on BO_4^{5-} anions, and there are two Fe^{3+} cations in the asymmetric unit, both of which are in (distorted) octahedral co-ordination.[39,40] The Fe^{3+}–O^- distances for the first Fe^{3+} cation range from 1·904 to 2·132 Å (mean 2·023 Å), and those for the second from 1·864 to 2·227 Å (mean 2·055 Å).[40] The B–O^- bond lengths for the BO_4^{5-} anions lie between 1·439 and 1·504 Å (mean 1·485 Å).[40]

No crystalline borate phases have been reported with tetrahedrally co-ordinated Fe^{3+} cations; i.e. with a network incorporating $Fe\emptyset_4^-$ structural units. A network with adjacent $B\emptyset_4^-$ and $Fe\emptyset_4^-$ structural units is unlikely to be stable, since both structural units are negatively charged, and so there are two possible locations for the tetrahedrally co-ordinated Fe^{3+} cations. Either the $Fe\emptyset_4^-$ units are incorporated into a network of trigonal borate structural units, or they are present in silicate chemical groupings, as in the case of the tetrahedrally co-ordinated Fe^{3+} cations in the soda–lime–silica glass of Ref. 5. In either case, the negative charge on the $Fe\emptyset_4^-$ structural units must be balanced by a positively charged Na^+ network modifying cation. However, there appear to be no crystalline Na_2O–Fe_2O_3–B_2O_3 crystalline phases, which strongly suggests that the tetrahedrally co-ordinated Fe^{3+} cations are almost certainly located in silicate chemical groupings. The slight increase in the average bond length for the Si(O) peak may be due to the replacement of Si–O^- bonds to nonbridging oxygen atoms with Si–Ø–Fe linkages to $Fe\emptyset_4^-$ tetrahedra.

Given that the tetrahedrally co-ordinated Fe^{3+} cations seem to be associated with silicate chemical groupings, combined with the fact that there are no known Na_2O–Fe_2O_3–B_2O_3 crystalline phases, leads to the conclusion that the Fe^{3+} cations are most likely to be present in $FeBO_3$ chemical groupings; i.e. as octahedrally co-ordinated Fe^{3+} cations associated with BO_3^{3-} orthoborate anions. The boundaries between the $FeBO_3$ chemical groupings and the other chemical groupings that make up the borosilicate network would then involve $BO_2Ø^{2-}$, $BOØ_2^-$ and possibly $SiOØ_3^-$ basic structural units. This association of the octahedrally co-ordinated Fe^{3+} "network-modifying" cations with isolated BO_3^{3-} orthoborate anions, rather than a borate network, is entirely consistent with the presence of $B_2O_5^{4-}$ pyroborate anions in Region 4 of the Dell *et al*[7] model; i.e. at the highest network-modifying cation content. As a result, the octahedrally co-ordinated Fe^{3+} cations will be much more easily leached than those that are tetrahedrally co-ordinated, and incorporated into the network of silicate chemical groupings.

Finally, the question arises as to the location of the octahedrally co-ordinated Fe^{2+} cations. The only crystalline ferrous borate phase known to the authors is the pyroborate, $Fe_2B_2O_5$, which is isostructural with triclinic $Mg_2B_2O_5$, $Mn_2B_2O_5$ and $Co_2B_2O_5$.[41] The structure of $Mg_2B_2O_5$[41] is formed from Mg^{2+} cations and $B_2O_5^{4-}$ pyroborate anions, with two symmetrically-distinct Mg^{2+} cations octahedrally co-ordinated by oxygen atoms. One Mg^{2+} cation has six nonbridging oxygen atom neighbours, whereas the first co-ordination shell of the second includes five nonbridging and one bridging oxygen atom (the central oxygen atom of the pyroborate anion). Unfortunately, however, structural parameters (Fe–O distances) have not been reported for $Fe_2B_2O_5$, but the existence of this crystalline phase does suggest that the Fe^{2+} cations are associated with independent borate (pyroborate and/or orthoborate) anions. One possibility is that disorder within the $FeBO_3$ chemical groupings leads to non-stoichiometry, with some of the Fe^{3+} cations being replaced by Fe^{2+} cations.

4.4. Comparison with vitreous Na_2O–CaO–Fe_2O_3–SiO_2[5]

It is interesting to compare the effect of the added Fe_2O_3 on the structure of the present sodium borosilicate glass with that on the structure of the soda–lime–silica glass in Ref. 5. The $\Delta T_X(r)$ – base glass difference correlation functions, $\Delta T(r)$, for the two glasses are shown in Figure 11, and $\Delta T_{Fe}(r)$ in Figure 12. Whilst the peak positions and structure in $\Delta T(r)$ at higher r (Figure 11; r>4 Å) are remarkably similar, two important differences are worthy of note in respect of the present glasses: First, the structure in $\Delta T(r)$ around the first peak in $T(r)$ for the corresponding base glass is considerably more pronounced, reflecting the much greater change in the distribution of basic structural unit species; i.e. the conversion of negatively-charged $BØ_4^-$ tetrahedra into triangular borate structural units with nonbridging oxygen atoms. Second, the average density contribution to $\Delta T(r)$ is negative, whereas it is positive for the soda–lime–silica glasses. This is consistent with the fact that, for the sodium borosilicate glass, the average atomic number density decreases from 0·08116 to 0·07821 atoms $Å^{-3}$ on the addition of Fe_2O_3 but, for the soda–lime–silica glass,[5] it increases from 0·07278 to 0·07497 atoms $Å^{-3}$.

A much better guide as to the effect of the addition of Fe_2O_3 on the vitreous network is to consider the average network number density $\rho_N°$, which is the average number of network structural units (s.u.) per unit volume. In both cases, $\rho_N°$ decreases with the incorporation of the Fe_2O_3, as expected; i.e. the network expands to accommodate the Fe_2O_3. For the sodium borosilicate glass, it decreases by 19·7%, from 0·02348 to 0·01886 s.u. $Å^{-3}$, and for the soda–lime–silica glass it decreases by 16·5%, from 0·01823 to 0·01522 s.u. $Å^{-3}$. (Note that these network number densities do not include

the $FeØ_4^-$ tetrahedra incorporated into the network of the Fe_2O_3-containing glasses.) A possible explanation for the slightly larger reduction for the present glasses is that the replacement of 4-connected $BØ_4^-$ tetrahedra by trigonal borate structural units with nonbridging oxygen atoms leads to a more open (less compact) network.

The Fe–Fe+Fe–X correlation function, $\Delta T_{Fe}(r)$, which mainly consists of Fe–X interactions, is also very similar to that for the Na_2O–CaO–Fe_2O_3–SiO_2 glass in Ref. 5, as may be seen from Figure 12. However, again there are some significant differences when the present Na_2O–Fe_2O_3–B_2O_3–SiO_2 glass is compared to vitreous Na_2O–CaO–Fe_2O_3–SiO_2:

1. The first (Fe–O) peak is at slightly lower *r*, with an increased area, but the peak widths are very similar, reflecting the lower Fe^{3+} fraction and the fact that the octahedrally co-ordinated Fe^{3+}/Fe^{2+} cations are now incorporated into borate chemical groupings.
2. The maximum of the peak between 3·0 and 3·5 Å, which mainly involves Fe–Na, Fe–B and Fe–Si distances, is at lower *r*, and the peak has an increased width, due to the presence of Fe–B interactions.
3. The {predominantly Fe–(2)O} peak at 4·4 Å is also broader, with the suggestion of a low-*r* shoulder, although the position of the maximum is exactly the same (4·41 Å), as a result of the wider range of Fe^{3+} cation environments.
4. The average density contribution to $\Delta T_{Fe}(r)$ is larger, due to the combined effect of the higher atomic number density, ρ°, and the different neutron scattering lengths, *b*, for the constituent atoms.

All of these differences can be accounted for by the fact that the Fe^{3+}/Fe^{2+} cations are now present in both borate and silicate chemical groupings, rather than just silicate chemical groupings, as in the case of the Na_2O–CaO–Fe_2O_3–SiO_2 glass.[5]

5. Conclusions

It can therefore be concluded that the present data for the Fe_2O_3-containing Na_2O–$^{11}B_2O_3$–SiO_2 glasses are consistent with a fraction of 0·45±0·10 of the iron being present as network-forming $FeØ_4^-$ tetrahedra, each associated with an Na^+ network-modifying cation. The remaining iron is most likely to be predominantly in octahedral co-ordination, and exists as both Fe^{3+} (0·48±0·10) and Fe^{2+} (0·07±0·01) network-modifying cations. However, the presence of a minor fraction of 5-fold co-ordinated Fe^{2+} and/or Fe^{3+} network-modifying cations cannot be eliminated.

The chemical nanoheterogeneity of borosilicate glasses may be thought of as consisting of a transition from B_2O_3 regions containing boroxol groups, through borate regions containing superstructural units such as triborate, pentaborate and diborate groups, followed by borosilicate regions with 4-membered rings similar to those in danburite and reedmergnerite, then silicate regions involving $Si^{[3]}$ and $Si^{[4]}$ basic structural units, and finally to SiO_2 regions with only $Si^{[4]}$ units. The presence and relative dimensions of these various regions depends on the overall composition and thermodynamic balance. In the case of the sodium borosilicate glass in this study, the thermodynamic modelling predicts the absence of B_2O_3 chemical groupings, but that 25% of the boron atoms are present as $B^{[3]}$ and 20% as $B^{[4]}$ in borate groupings, and that the remaining 55% are involved in borosilicate groupings, which is consistent with the ^{11}B NMR data. The model also predicts that 45% of the silicon atoms are present as $Si^{[4]}$ in borosilicate groupings, 23% as $Si^{[3]}$ units and 1% as $Si^{[4]}$ in silicate groupings, and 31% as $Si^{[4]}$ in SiO_2 groupings. This is similarly consistent with the ^{29}Si NMR data. (Note, however, that this comparison of the thermodynamic

modelling and NMR data ignores the presence of the $BO\emptyset_2^-$ and $SiO_2\emptyset_2^{2-}$ basic structural units predicted by the former, but which were below the detection limit of the NMR spectroscopy, and also that the present glass is outside the phase-separation region.)

On the addition of Fe_2O_3, the base glass borosilicate network expands to accommodate the Fe^{3+}/Fe^{2+} cations. This expansion is greater than that for the soda–lime–silica glass of Ref. 5, due to the conversion of negatively charged $B\emptyset_4^-$ tetrahedra into trigonal borate structural units incorporating nonbridging oxygen atoms. The most likely scenario for the inclusion of the Fe_2O_3 into the base glass structure is that the tetrahedrally co-ordinated Fe^{3+} cations form $Fe\emptyset_4^-$ structural units that are incorporated into the network of silicate chemical groupings, whereas more easily leached Fe^{3+} cations in octahedral co-ordination are present as $FeBO_4$ chemical groupings, consisting of Fe^{3+} cations plus BO_3^{3-} orthoborate anions, which may become non-stoichiometric due to the presence of Fe^{2+} cations. The fact that network-modifying Fe^{3+}/Fe^{2+} cations are located within borate chemical groupings has implications for the long-term leachability of vitrified nuclear and other toxic wastes.

Finally, it is interesting to note that the relative ease with which foreign cations can be incorporated into the sodium borate component of a sodium borosilicate glass is reminiscent of the well-known borax bead test used in qualitative chemical analysis. The compound containing an unknown cation is melted together with borax ($Na_2B_4O_7.10H_2O$) and cooled to form a glass bead in a platinum wire loop, the colour of this bead being characteristic of the unknown cation.

Acknowledgements

This work was supported financially by BNFL, who also funded purchase of the isotopically-enriched $^{57}Fe_2O_3$, and the UK EPSRC, and JLS and RH would like to thank BNFL and the EPSRC, respectively, for PhD studentships. The authors are also grateful to the Institut Laue-Langevin for neutron beam time and experimental assistance. The NMR facilities employed in this study were part funded by Birmingham Science City Advanced Materials Projects 1 and 2, supported by Advantage West Midlands (AWM) and the European Regional Development Fund (ERDF).

References

1. Parkinson, B. G., Holland, D., Smith, M. E., Larson, C., Doerr, J., Affatigato, M., Feller, S. A., Howes, A. P. & Scales, C. R. *J. Non-Cryst. Solids*, 2008, **354**, 1936.
2. Duddridge, A. *PhD Thesis*, University of Warwick, 2004.
3. Holland, D., Parkinson, B. G., Islam, M. M., Duddridge, A., Roderick, J. M., Howes, A. P. & Scales, C. R. *Appl. Magn. Reson.*, 2007, **32**, 483.
4. Wright, A. C., Sinclair, R. N., Shaw, J. L., Haworth, R., Scales, C. R., Cuello, G. J. & Vedishcheva, N. M. *Phys. Chem. Glasses: Eur. J. Glass Sci. Technol. B*, 2017, **58**, xxx accompanying paper (PCG-D-16-00015).
5. Wright, A. C., Clarke, S. J., Howard, C. K., Bingham, P. A., Forder, S. D., Holland, D., Martlew, D. & Fischer, H. E. *Phys. Chem. Glasses: Eur. J. Glass Sci. Technol. B*, 2014, **55**, 243.
6. Vedishcheva, N. M. & Wright, A. C. In: *Glass: Selected Properties and Crystallization*, Ed. J. W. P. Schmelzer, de Gruyter, Berlin, 2014, Chapter 5, p. 269.
7. Dell, W. J., Bray P. J. & Xiao, S. Z. *J. Non-Cryst. Solids*, 1983, **58**, 1.
8. Shaw, J. L., Wright, A. C., Sinclair, R. N., Kiczenski, T. J., Feller, H. A., Feller, S. A. & Scales, C. R. *Phys. Chem. Glasses*, 2002, **43C**, 59.
9. Vedishcheva, N. M., Shakhmatkin, B. A. & Wright, A. C. *Phys. Chem. Glasses*, 2003, **44**, 191.
10. Wright, A. C., Shaw, J. L., Sinclair, R. N., Vedishcheva, N. M., Shakhmatkin, B. A. & Scales, C. R. *J. Non-Cryst. Solids*, 2004, **345&346**, 24.
11. Sears, V. F. *Neutron News*, 1992, **3**, 26.
12. Fischer, H. E., Palleau, P. & Feltin, D. *Physica B*, 2000, **276&278**, 93.

13. Fischer, H. E., Cuello, G. J., Palleau, P., Feltin, D., Barnes, A. C., Badyal, Y. S. & Simonson, J. M. *Appl. Phys. A: Mater. Sci. Process.*, 2002, **74** [Suppl.], S160.
14. Brown, P. J. *Magnetic Form Factors*, In: *Neutron Data Booklet*, Eds A.-J. Dianoux & G. Lander, Institut Laue-Langevin, Genoble, 2002, p. 2.5-1.
15. Massiot, D., Fayon, F., Capron, M., King, I., Le Calve, S., Alonso, B., Durand, J. O., Bujoli, B., Gan, Z. & Hoatson, G. *Magn. Reson. Chem.*, 2002, **340**, 76.
16. Vedishcheva, N. M., Shakhmatkin, B. A. & Wright, A. C. *J. Non-Cryst. Solids*, 2004, **345&346**, 39.
17. Vedishcheva, N. M., Polyakova, I. G. & Wright, A. C. *Phys. Chem. Glasses: Eur. J. Glass Sci. Technol. B*, 2014, **55**, 225.
18. Howes, A. P., Vedishcheva, N. M., Samoson, A., Hanna, J. V., Smith, M. E., Holland, D. & Dupree, R. *Phys. Chem. Chem. Phys.*, 2011, **13**, 11919.
19. Massiot, D., Bessada, C., Coutures, J. P. & Taulelle, F. *J. Magn. Reson.*, 1990, **90**, 231.
20. Du, L.-S. & Stebbins, J. F. *J. Phys. Chem.*, 2003, **B107**, 10063.
21. Wright, A. C., Vedishcheva, N. M. & Shakhmatkin, B. A. *Phys. Chem. Glasses: Eur. J. Glass Sci. Technol. B*, 2006, **47**, 497.
22. Wright, A. C., Sinclair, R. N., Stone, C. E., Shaw, J. L., Feller, S. A., Kiczenski, T. J., Williams, R. B., Berger, H. A., Fischer, H. E. & Vedishcheva, N. M. *Phys. Chem. Glasses: Eur. J. Glass Sci. Technol. B*, 2012, **53**, 191.
23. Smuts, J., Steyn, G. D. & Boeyens, J. C. A. *Acta Crystallogr.*, 1969, **B25**, 1251.
24. Zhong, J. H., Wu, X. W., Liu, M. L. & Bray, P. J. *J. Non-Cryst. Solids*, 1988, **107**, 81.
25. Bunker, B. C., Tallant, D. R., Kirkpatrick, R. J. & Turner, G. L. *Phys. Chem. Glasses*, 1990, **31**, 30.
26. Parkinson, B. G. *PhD Thesis*, University of Warwick, 2007.
27. Dyar, M. D., Agresti, D. G., Schaefer, M. W., Grant, C. A. & Sklute, E. C. Mössbauer Spectroscopy of Earth and Planetary Materials, In: *Ann. Rev. Earth Planet. Sci.*, 2006, **34**, 83.
28. Wilke, M., Farges, F. F., Petit, P.-E., Brown Jr. G. E. & Martin, F. *Am. Miner.*, 2001, **86**, 714.
29. Rossano, S., Ramos, A., Delaye, J.-M., Creux, S., Filipponi, A., Brouder, C. & Calas, G. *Europhys. Lett.*, 2000, **49**, 597.
30. Rossano, S., Ramos, A. Y. & Delaye, J.-M. *J. Non-Cryst. Solids*, 2000, **273**, 48.
31. Weigel, C., Cormier, L., Galoisy, L., Calas, G., Bowron, D. T. & Beuneu, B. *Appl. Phys. Lett.*, 2006, **89**, 141911.
32. Weigel, C., Cormier, L., Calas, G., Galoisy, L. & Bowron, D. T. *J. Non-Cryst. Solids*, 2008, **354**, 5378.
33. Weigel, C., Cormier, L., Calas, G., Galoisy, L. & Bowron, D. T. *Phys. Rev.*, 2008, **B78**, 064202.
34. Hayes, T. M. & Wright, A. C. In: *The Structure of Non-Crystalline Materials 1982*, Eds P. H. Gaskell, J. M. Parker & E. A. Davis, Taylor & Francis, London, 1983, p. 108.
35. Pant A. K. & Cruickshank, D. W. J. *Acta Crystallogr.*, 1968, **B24**, 13.
36. Pant, A. K. *Acta Crystallogr.*, 1968, **B24**, 1077.
37. Bernal, I., Struck, C. W. & White, J. G. *Acta Crystallogr.*, 1963, **16**, 849.
38. Diehl, R. *Solid State Commun.*, 1975, **17**, 743.
39. White, J. G., Miller, A. & Nielsen, R. E. *Acta Crystallogr.*, 1965, **19**, 1060.
40. Diehl, R. & Brandt, G. *Acta Crystallogr.*, 1975, **B31**, 1662.
41. Block, S., Burley, G., Perloff, A. & Mason Jr., R. D. *J. Res. NBS*, 1959, **62**, 95.

Table 1. Neutron scattering lengths[11] and sample compositions

Element	b (10^{-14} m)	Atom fraction (±0·0005)	
		Base glass	Fe-containing glasses
Na	0·363±0·002	0·1246	0·1039
^{NAT}Fe (^{57}Fe)	0·945±0·002 (0·284±0·010)	-	0·0675
^{11}B	0·659±0·004	0·1098	0·0915
Si	0·41491±0·00010	0·1795	0·1497
O	0·5803±0·0004	0·5861	0·5874

Table 2. Chemical structure of the base glass from thermodynamic modelling

Chemical grouping	Fraction (± 0·03)
$Na_2O.3B_2O_3$	0·01
$Na_2O.2B_2O_3$	0·08
$Na_2O.B_2O_3$	0·01
$Na_2O.B_2O_3.2SiO_2$	0·18
$Na_2O.B_2O_3.6SiO_2$	0·06
$3Na_2O.8SiO_2$	0·01
$Na_2O.2SiO_2$	0·15
$Na_2O.SiO_2$	0·01
SiO_2	0·49
Total	1·00

Table 3. Structural unit fractions from thermodynamic modelling (±0·03) and NMR spectroscopy (±0·015)

Structural unit	Borate	Silicate	Overall	NMR
$BØ_4^-$	0·72	-	0·27	0·285
$BØ_3$	0·25	-	0·10	0·094
$BOØ_2^-$	0·03	-	0·01	-
$SiØ_4$	-	0·77	0·48	0·475
$SiOØ_3^-$	-	0·22	0·13	0·146
$SiO_2Ø_2^{2-}$	-	0·01	0·01	-
Total	1·00	1·00	1·00	1·000

Table 4. Parameters obtained from fitting the ^{29}Si spectrum of the base glass. The intensities include the contributions from the spinning sidebands. During the fitting procedure, the half-widths of the spinning sidebands were constrained to be similar to the centreband peaks

Species	Isotropic shift (ppm ±1)	FWHM (ppm ±1)	Intensity (% ±2)
$Si^{[4]}(nB)^{*}$	–100	18	75
$Si^{[3]}$	–88	14	25

* $n \sim 1{\cdot}3$, see text.

Table 5. Fit to the ^{11}B MAS NMR spectrum

Species	Isotropic shift (ppm)	C_Q (MHz)	η_Q (fixed)	Relative intensity* (%)
$B^{[3]}_{ring}$	17·6	2·58	0·2	13
$B^{[3]}_{non\text{-}ring}$	15·1	2·44	0·2	11
$B^{[4]}$(B,3Si)	–1·5	-	-	56
$B^{[4]}$(4Si)	–2·2	-	-	20

* As fitted, and uncorrected for the $B^{[3]}$ intensity loss into sidebands.

Table 6. Average bond lengths in independent borate and silicate structural units, calculated from the data in Table 2 of Ref. 10

Borate units	B–Ø (Å)	B–O$^-$ (Å)
$BØ_4^-$	1·468	-
$BØ_3$	1·368	-
$BOØ_2^-$	1·400	1·324
$BO_2Ø^{2-}$	1·438	1·358
BO_3^{3-}	-	1·383
Silicate units	**Si–Ø (Å)**	**Si–O$^-$ (Å)**
$SiØ_4$	1·607	-
$SiOØ_3^-$	1·639	1·570
$SiO_2Ø_2^{2-}$	1·675	1·592
$SiO_3Ø^{3-}$	1·682	1·622
SiO_4^{4-}	-	1·640

Table 7. Base glass and $\Delta T_X(r)$ peak fit parameters

Fit	r_{B-O} (Å)	$\langle u_{B-O}^2\rangle^{½}$ (Å)	$n_{B(O)}$	r_{Si-O} (Å)	$\langle u_{Si-O}^2\rangle^{½}$ (Å)	$n_{Si(O)}$	R_χ
$T(r)$	1·477	0·103	3·89	1·617	0·071	3·96	0·021
$\Delta T_X(r)$	1·427	0·094	3·43	1·627	0·053	3·97	0·015

Table 8. Peak fit parameters for the first (Fe–O) peak in $\Delta T_{Fe}(r)$

r_{Fe-O} (Å)	$\langle u_{Fe-O}^2\rangle^{½}$ (Å)	$n_{Fe(O)}$
1·895±0·002	0·079±0·010	4·30±0·20
2·182±0·030	0·041±0·010	0·58±0·20

Table 9. Calculation of the average Si(B) co-ordination number, n_{SiB}, using the thermodynamic prediction for the chemical groupings in the base glass

	Chemical groupings						Overall fraction	n_{SiB}
	$Na_2O.B_2O_3.2SiO_2$	$Na_2O.B_2O_3.6SiO_2$	$3Na_2O.8SiO_2$	$Na_2O.2SiO_2$	$Na_2O.SiO_2$	SiO_2		
n_{SiB}	3	4/3	0	0	0	0	-	-
$Si^{[4]}$	2×0·18	6×0·06	2×0·01	-	-	0·49	0·769	1·27
$Si^{[3]}$	-	-	6×0·01	2×0·15	-		0·225	0
$Si^{[2]}$	-	-	-	-	0·01		0·006	0

Figure Captions

Figure 1. Neutron diffraction data reduction for the $^{NAT}Fe_2O_3$-containing glass. Top, raw diffraction pattern (points) with cubic-spline fit (solid line); centre, corrected, normalised diffraction pattern, I(Q) *(solid line), and the paramagnetic plus self-scattering (dashed line) and bottom, the interference function,* Qi(Q)

Figure 2. (A) Lorentzian and (B) Extended Voigt-based (xVBF) fits to the Mössbauer spectrum for the $^{NAT}Fe_2O_3$-containing glass

Figure 3. Corrected, normalised diffraction patterns, I(Q)*, for the $^{NAT}Fe_2O_3$- and $^{57}Fe_2O_3$-containing samples, together with that for the base glass*

Figure 4. Real-space total correlation functions, T(r)*, for the* $^{NAT}Fe_2O_3$- *and* $^{57}Fe_2O_3$*-containing samples, with their difference,* ΔT(r)

Figure 5. The Fe–Fe+X–X and base glass real-space total correlation functions plus their difference, ΔT(r)*. Note that* $\Delta T_X(r)$ *is divided by the base glass fraction (0·88) to allow subtraction of the base glass correlation function to give* $\Delta T(r)$

Figure 6. Gaussian fits to the ^{29}Si MAS NMR spectrum for the base glass (Larmor frequency 59·6 MHz; MAS frequency 4·5 kHz. Points, data; solid blue lines, peak fits and solid red line, summed fit)

Figure 7. Simulation of the ^{11}B MAS NMR spectrum for the base glass (points, data; solid and dashed blue lines, peak fits and solid red line, summed fit)

Figure 8. Two-peak fit (Table 7) to the first (B–O+Si–O) peak in (A) the experimental real-space correlation function, T(r)*, for the base glass, and (B) the Fe–Fe+X–X difference correlation function,* $\Delta T_X(r)$*, (——, experiment; – – – –, fit; · · · · ·, individual peaks and – · – · –, residual)*

Figure 9. Two-peak fit (Table 8) to the first (Fe–O) peak in the Fe–Fe+Fe–X difference correlation function, $\Delta T_{Fe}(r)$*. (Key as Figure 8)*

Figure 10. Running Fe(O) co-ordination number between 1·5 Å and r*, obtained from the area under* $r\Delta T_{Fe}(r)$

Figure 11. The $\Delta T_X(r)$ *– base glass difference correlation functions,* ΔT(r)*, for the present glasses (solid line), together with that for the soda–lime–silica system from Ref. 5 (dashed line)*

Figure 12. A comparison of the Fe–Fe+Fe–X difference correlation functions, $\Delta T_{Fe}(r)$*, for the present glass (solid line) with that for vitreous $Na_2O–CaO–Fe_2O_3–SiO_2$ [5] (dashed line)*

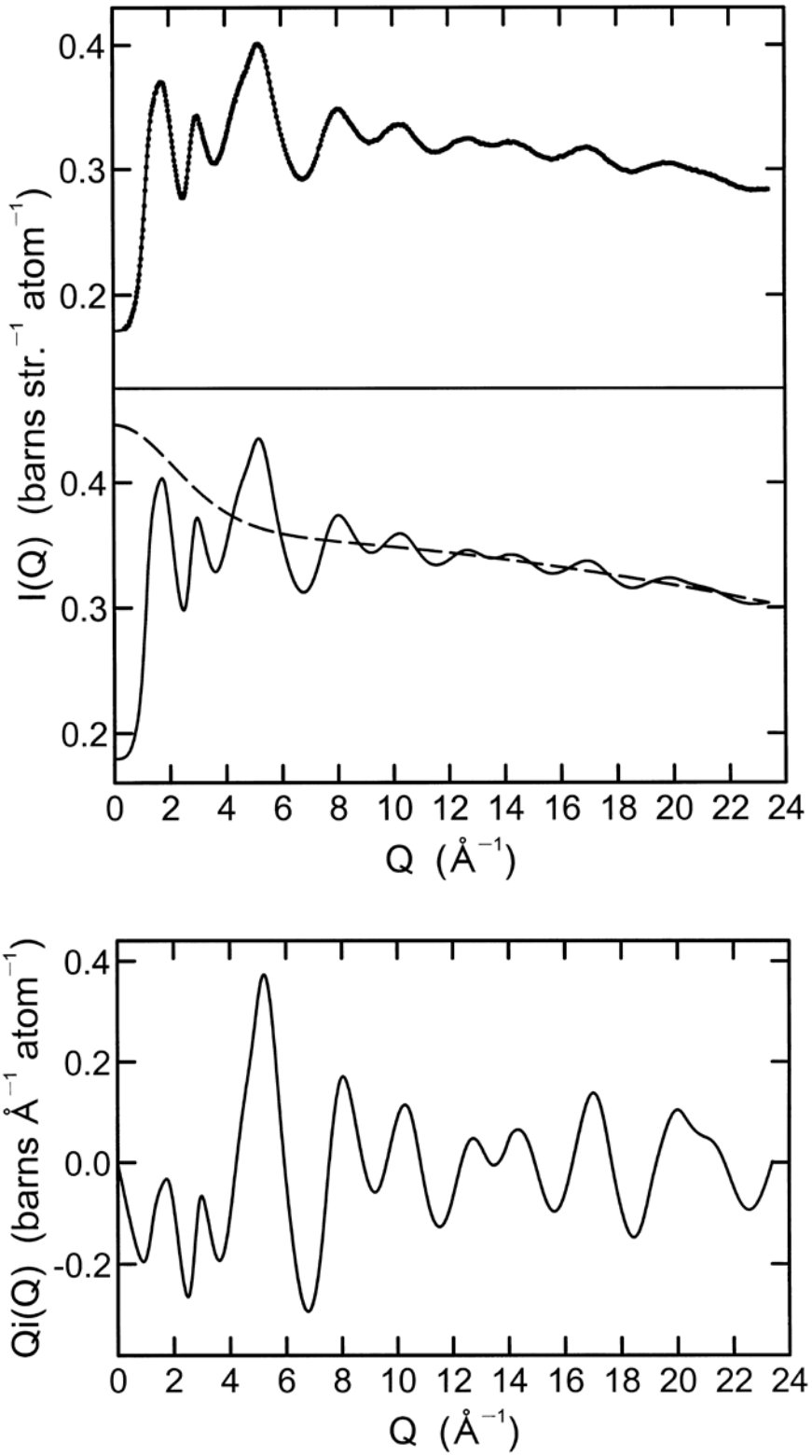
0.4
0.3
0.2
I(Q) (barns str.$^{-1}$ atom^{-1})
0.4
0.3
0.2
0 2 4 6 8 10 12 14 16 18 20 22 24
Q (Å^{-1})
0.4
0.2
0.0
-0.2
Qi(Q) (barns Å^{-1} atom^{-1})
0 2 4 6 8 10 12 14 16 18 20 22 24
Q (Å^{-1})

Figure 1.

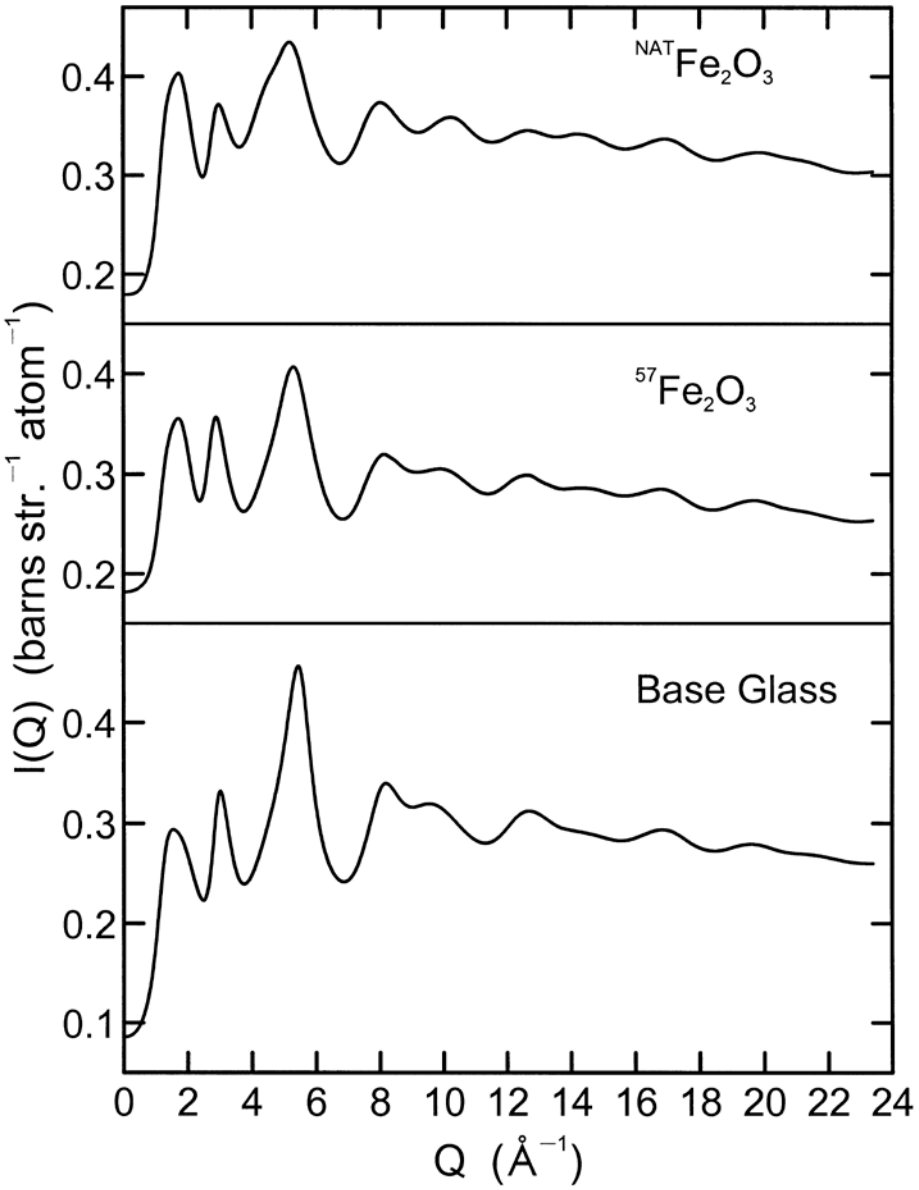
$^{NAT}Fe_2O_3$
$^{57}Fe_2O_3$
Base Glass
I(Q) (barns str.$^{-1}$ atom^{-1})
Q (Å^{-1})
0.1
0.2
0.3
0.4
0 2 4 6 8 10 12 14 16 18 20 22 24

Figure 3.

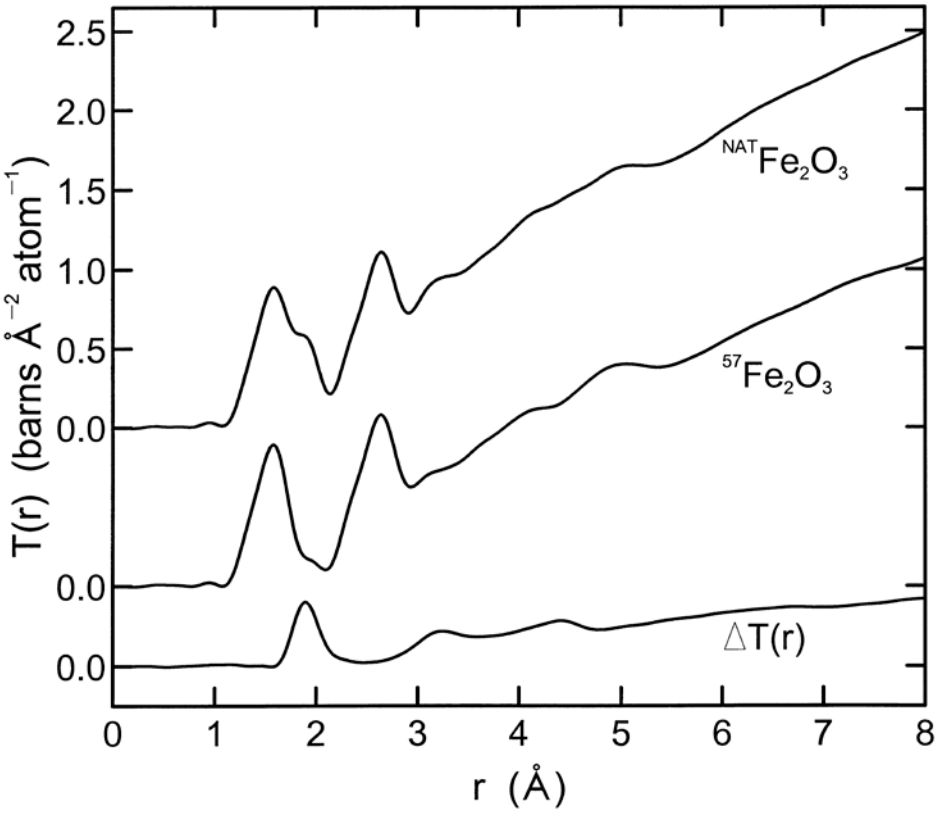
2.5
2.0
1.5
1.0
0.5
0.0
0.0
0.0
T(r) (barns Å^{-2} atom^{-1})
$^{NAT}Fe_2O_3$
$^{57}Fe_2O_3$
△T(r)
0
1
2
3
4
5
6
7
8
r (Å)

Figure 4.

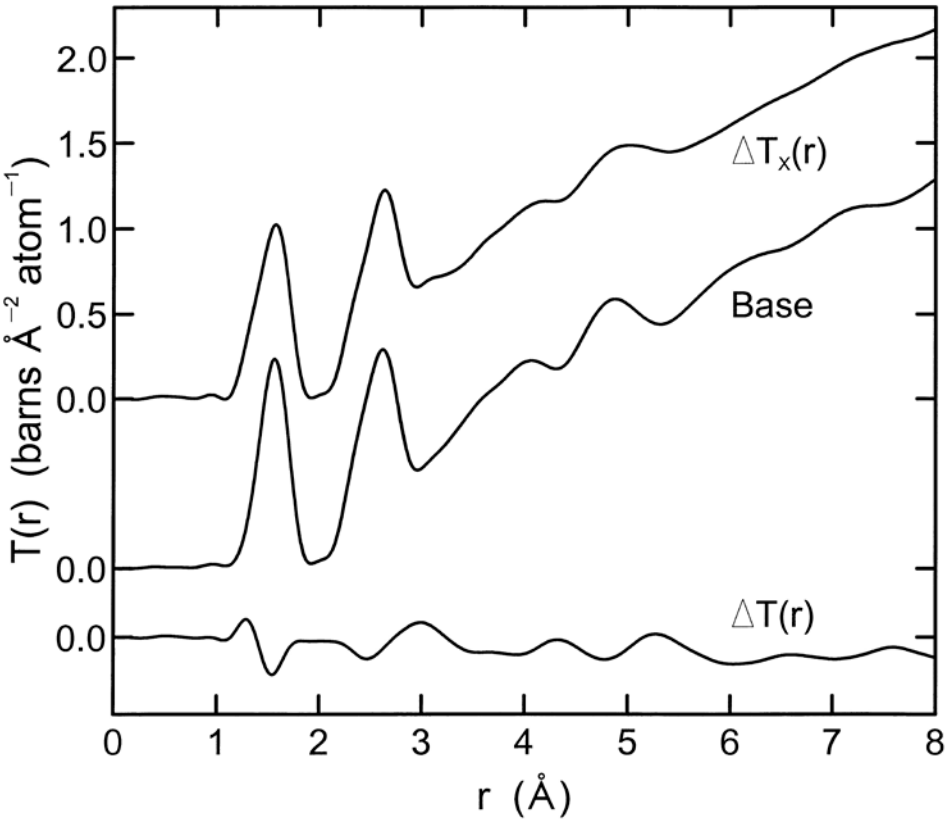

Figure 5.

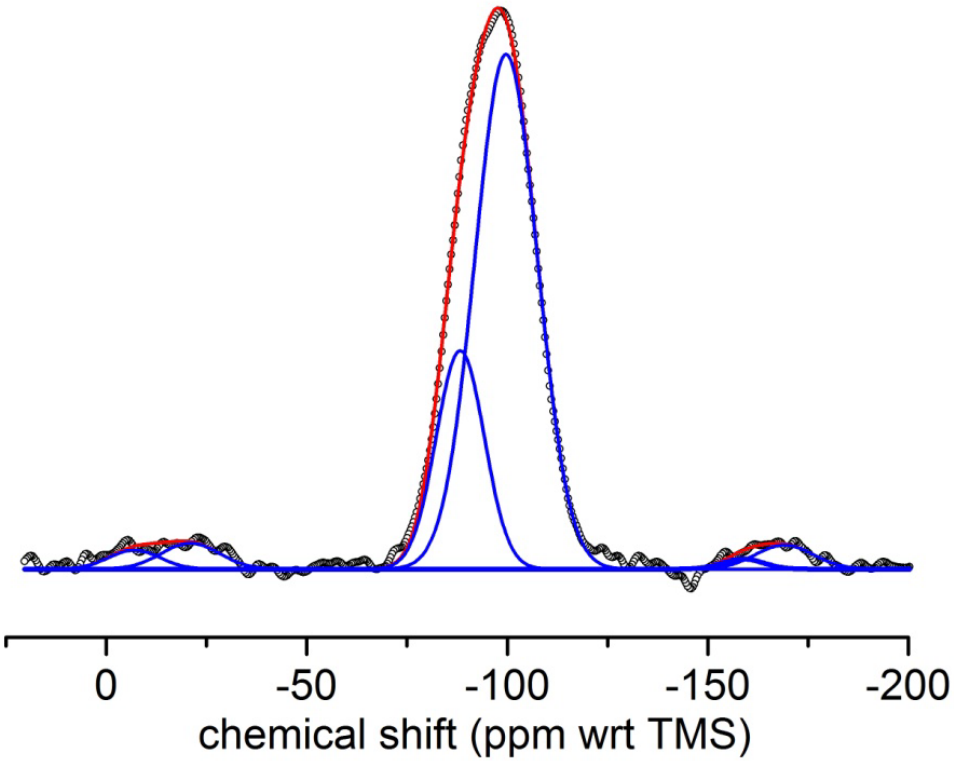

Figure 6.

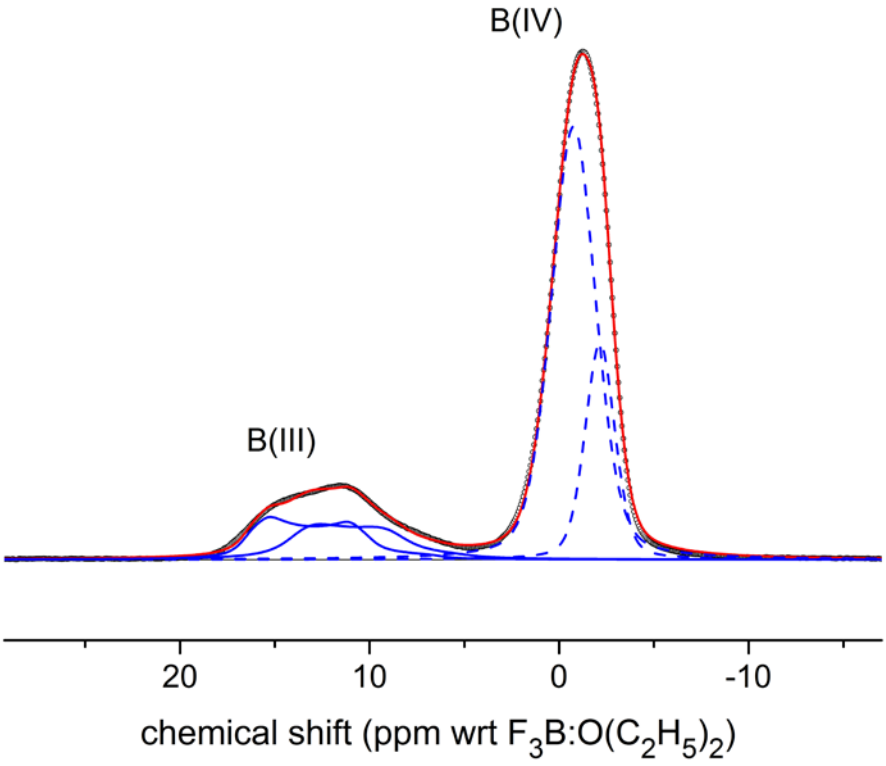

Figure 7.

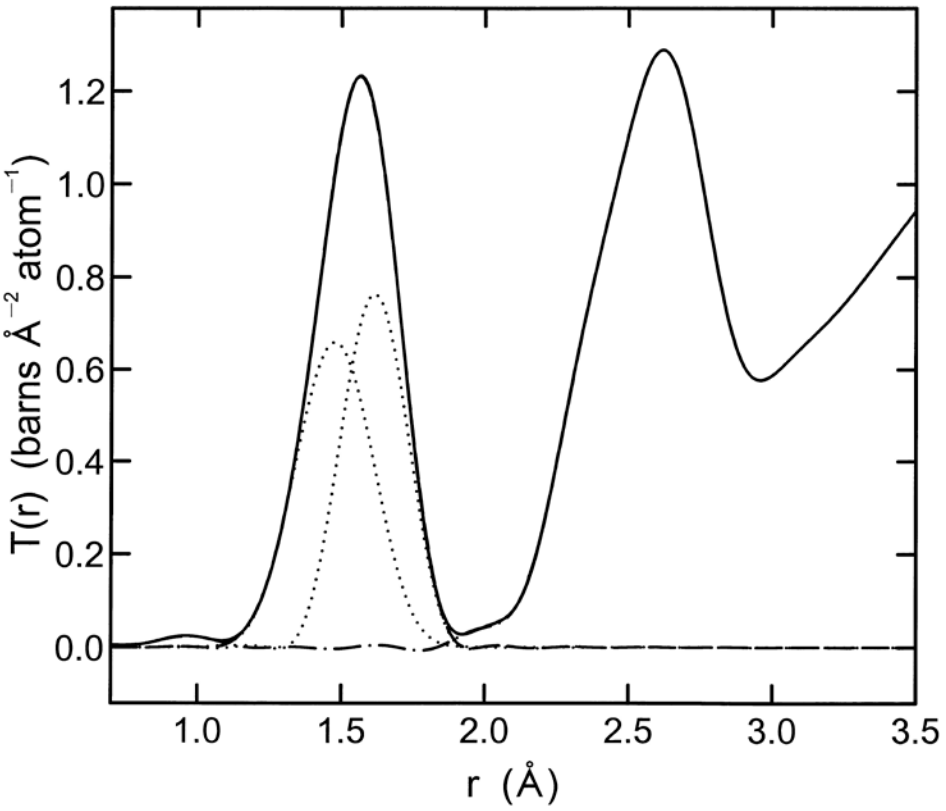

Figure 8(A).

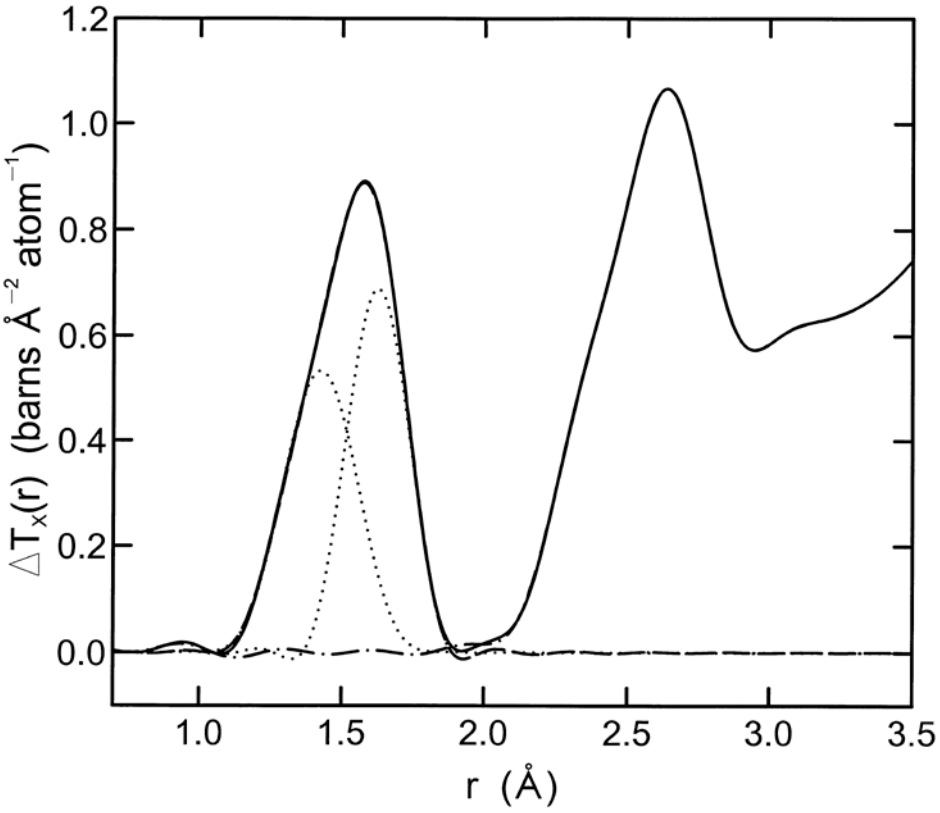

Figure 8(B).

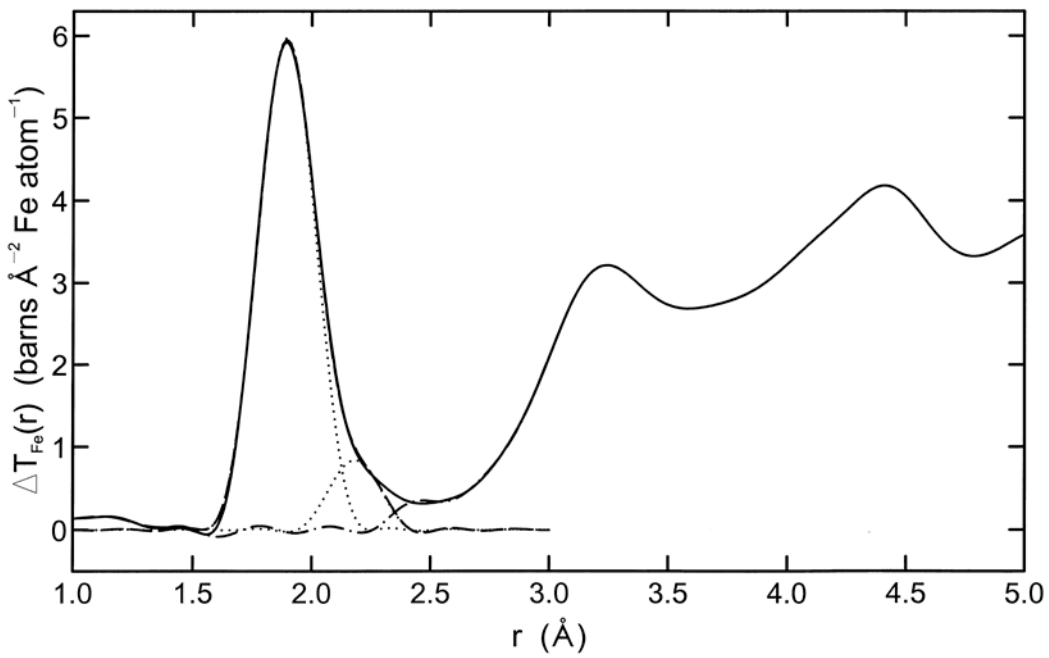

Figure 9.

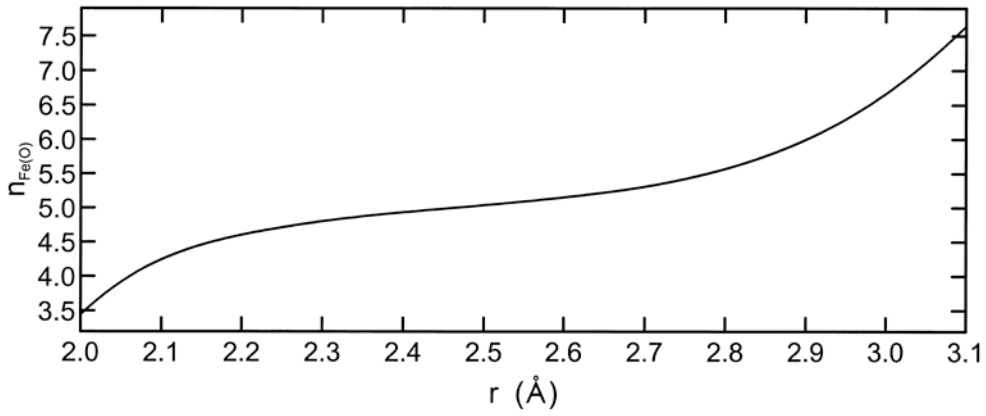

Figure 10.